Porous Fairings for Landing Gear Noise Mitigation

Original
Porous Fairings for Landing Gear Noise Mitigation / Gondrum, Miro; Meinke, Matthias; Schroeder, Wolfgang; Avallone, Francesco; Ragni, Daniele. - (2024). (30th AIAA/CEAS Aeroacoustics Conference (2024) Rome (ITA) June 4-7, 2024) [10.2514/6.2024-3174].

Publisher:
American Institute of Aeronautics and Astronautics

Published
DOI:10.2514/6.2024-3174

Porous fairings for landing gear noise mitigation

Miro Gondrum[*], Matthias Meinke[†], and Wolfgang Schröder[‡]
Chair of Fluid Mechanics and Institute of Aerodynamics, RWTH Aachen University,
Wüllnerstr. 5a, 52062 Aachen, Germany

Francesco Avallone [§]
Dipartimento di Ingegneria Meccanica e Aerospaziale, Politecnico di Torino,
Corso Duca degli Abruzzi 24, 10129 Torino, Italy

Daniele Ragni [¶]
Faculty of Aerospace Engineering, Delft University of Technology,
Kluyverweg 1, 2629 HS Delft, The Netherlands

The noise emission of a simplified two-wheel nose landing gear configuration featuring a detachable porous fairing is investigated by a hybrid CFD/CAA approach. The noise mitigation properties of the porous fairing are discussed and compared against two reference configurations, i.e., baseline configurations with and without a solid fairing. The time resolved flow and acoustic near field is computed by a lattice Boltzmann (LB) method with a collision step based on countable cumulants, and the noise radiation into the far field is predicted by solving a permeable surface Ffowcs Williams and Hawkings formulation. The porous material is represented by an equivalent forcing term in the LB equation based on a Forchheimer-extended Darcy model. The porous material has a deterministic geometric structure such that the modeling parameters describing the porous material properties are determined by results from a flow simulation through the resolved micro-structures in a periodic pressure drop setup. The effect of the different fairings on the flow field and the resulting acoustic far field pressure are discussed.

I. Nomenclature

c_s = speed of sound
f = particle probability distribution function
p = pressure
s = wall distance function to FWH surface
r = level of refinement
t = time
w_j = weights for discrete equilibrium function j
$\mathrm{C}_1, \mathrm{C}_2$ = parameters for modeling the drag force
D = landing gear wheel diameter
$G(\cdot;\cdot)$ = Green's function
$H(\cdot)$ = Heaviside step function
L = domain reference length
L_f = thickness of the fairing
M = Mach number
Re = Reynolds number
$\underline{c}_j$ = discrete particle velocity j
$\underline{u}$ = flow velocity vector
$\underline{v}$ = FWH surface velocity vector
$\underline{x}$ = space coordinate
$\underline{y_o}$ = observer coordinate
$\underline{y_s}$ = source coordinate
$\underline{F}$ = volume force vector
$\underline{\underline{I}}$ = identity matrix
$\underline{\underline{P}}$ = compressive stress tensor
$\underline{\underline{T}}$ = Lighthill's stress tensor
δ_{ij} = Kronecker delta
ϵ = perturbation parameter
ν = viscosity
ρ = density
ϕ = porosity
ω = relaxation rate
Ω = collision operator
$\underline{\xi}$ = particle velocity
Δt = computational time step
Δx_r = grid spacing on the refinment level r

---

[*] Research Scientist, RWTH Aachen University, m.gondrum@aia.rwth-aachen.de.
[†] Senior Scientist, RWTH Aachen University, AIAA member, m.meinke@aia.rwth-aachen.de.
[‡] Professor, RWTH Aachen University, AIAA member, office@aia.rwth-aachen.de.
[§] Professor, Politecnico di Torino, AIAA member, francesco.avallone@polito.it
[¶] Associate Professor, Delft University of Technology, AIAA member, d.ragni@tudelft.nl

II. Introduction

For the development of future commercial aircraft, noise reduction technologies have become of utmost interest due to increasingly stringent airport emission regulations. During approach and landing, engines are operated almost under idle conditions. Thus, the noise contribution generated by airframe components such as landing gears (LG) becomes significant. The LG is an assembly of various blunt sub-components, each causing detached turbulent flow. Interactions between these wakes with downstream located LG sub-components are responsible for an LG typical broadband noise generation [1].

Simulations of the complex flow and acoustic fields by numerical methods helps to better understand the noise generating mechanisms and thus to develop strategies to mitigate them. The AIAA Benchmark problems for Airframe Noise Computations (BANC) define a simplified LAGOON nose LG configuration [2], which has been investigated by various numerical and experimental methods [2–5]. Thus, it serves as a well documented benchmark for the validation of numerical methods applied in this area. In recent investigations, it has been reported that the overall sound pressure level with an installed sub-component such as a torque link is increased by 5 dB [6]. However, the simplified LAGOON LG only consists of a main strut and two wheels with cavities making it unsuitable for the assessment of noise reduction technologies for broadband noise generation from wake-surface interactions.

In [7] a wire mesh screen has been placed upstream of a tandem cylinder configuration yielding a reduction of far field noise levels of about 5 dB. Noise mitigation also has been reported for fairings installed upstream of an LG. The noise reduction effect of a curved perforated fairing is compared to a similarly shaped solid fairing in [8]. It was shown that the noise reduction effect of such a perforated fairing is smaller than for a solid fairing, exhibiting, though, beneficial properties regarding weight and cooling air for the brakes. Similar observations have been made for a more realistic experimental study [9]. The findings showed that larger values of fairing porosity offered poorer noise mitigation properties. The authors concluded that a general design criterion is difficult to draw and more research on this topic is recommended.

To further analyze the effects of porous fairing on LG noise emission a more representative LG model as defined in the BANC case is needed. Therefore, the LG study presented in [10] is extended in this paper, by adding a porous fairing made of a material with a deterministic pore structure. The deterministic pore structure allows to perform scale resolved flow simulations through the porous micro-structures, to determine the coefficients for a homogeneous Darcy-Forchheimer model applied in this paper in a lattice Boltzmann method to predict the flow field and the effect on the acoustic field.

The remainder of this manuscript possesses the following structure: First, the applied computational methodologies, i.e., the cumulant lattice Boltzmann and the Ffowcs Williams and Hawkings methods, are summarized. In section IV geometry details of the investigated landing gear and porous material are given before describing the computational setup of the CFD/CAA simulation of the different landing gear configurations. Finally, in section V the influence of the different fairings on the flow and acoustic field is analysed.

III. Computational methodologies

The turbulent flow and the acoustic near field is predicted by a lattice Boltzmann (LB) method. To efficiently predict the acoustic far field, the Ffowcs Williams and Hawkings (FWH) equation is solved in a post processing step. Its input data, i.e., the time history of the pressure signal on a pre-defined permeable FWH surface, is extracted from the LB solution. Both methods are implemented in the multiphysics solver framework m-AIA, which is developed at the Institute of Aerodynamics of RWTH Aachen University.

A. Cumulant lattice Boltzmann method

The Boltzmann equation describes the temporal evolution of the particle probability density function (PPDF) $f(\underline{x}, \underline{\xi}, t)$, which represents the probability to find a particle at a certain position in momentum space, i.e., around a location $\underline{x}$, at a given time t with a particle velocity $\underline{\xi}$. The Boltzmann equation reads

$$\frac{\partial f}{\partial t} + \underline{\xi} \cdot \nabla_x f + \frac{\underline{F}}{\rho} \cdot \nabla_\xi f = \Omega(f), \tag{1}$$

with $\underline{F}$ representing an external force and the collision operator Ω accounts for the effect of the momentum exchange of particle collisions on the distribution function. Enskog demonstrated [11] through a series expansion of the momentum distribution function with the perturbation parameter ϵ, i.e., $f = f^{(0)} + \epsilon f^{(1)} + O(\epsilon^2)$, that a first-order approximation of the Boltzmann equation recovers the Navier-Stokes equations.

A discretization of eq. (1) results in the lattice Boltzmann equation

$$f_j(\underline{x} + \underline{c}_j \Delta t, t + \Delta t) = f_j^*(\underline{x}, t) = f_j(\underline{x}, t) + \Omega_j(f) + F_j \Delta t \,,$$

with the discrete particle velocity $\underline{c}_j = \underline{\xi}_j / \sqrt{3}$ in the discrete direction j. The asterisk ($*$) indicates the post-collision state. In the presented study, the particle velocity space is discretized in a three-dimensional Cartesian lattice featuring 27 discrete velocity directions, i.e., a D3Q27 model is used. Macroscopic flow quantities such as the density ρ and the flow velocity $\underline{u}$ are obtained from the moments of the PPDF incorporating the external forcing term. The discrete integrals read

$$\rho(\underline{x}, t) = \sum_j f_j(\underline{x}, t) + \frac{\Delta t}{2} \sum_j F_j \quad \text{and} \quad \underline{u}(\underline{x}, t) = \frac{1}{\rho} \sum_j \underline{c}_j f_j(\underline{x}, t) + \frac{\Delta t}{2\rho} \sum_j \underline{c}_j F_j \,.$$

Here, the fluid velocity is redefined containing the forcing term F_j as derived in [12]. The collision step, i.e., evaluating the collision operator, can be performed, e.g., by using the Bhatnagar-Gross-Krook (BGK) operator [13] or by a cumulant collision operator [14]. The former is widely used for low Reynolds number flow, whereas the latter has been shown to be more stable and accurate in predicting high Reynolds number flows, implying, however, additional computational effort. The BGK operator reads

$$\Omega_j = -\omega_{BGK}(f_j - f_j^{eq}),$$

where f_j^{eq} denotes the Maxwell equilibrium distribution function and ω_{BGK} the non-dimensional relaxation frequency

$$\omega_{BGK} = \frac{\Delta t c_s^2}{\nu_{eff} + \frac{1}{2} \Delta t c_s^2} \,. \tag{2}$$

The time step is Δt. The effective viscosity ν_{eff} represents the sum of the fluid viscosity, a turbulent viscosity calculated by a Smagorinsky sub-grid scale model [15], and an artificial viscosity introduced only in a sponge region near domain boundaries to reduce wave reflections. The equilibrium distribution for isothermal flow is approximated by a second-order expansion

$$f_j^{eq} = w_j \rho \left(1 + \frac{\underline{c}_i \cdot \underline{u}}{c_s^2} + \frac{\underline{u}\,\underline{u} : (\underline{c}_j\,\underline{c}_j - c_s^2 \underline{\underline{I}})}{2 c_s^4 \phi} \right) , \tag{3}$$

where the weighting factors w_j are equal to 8/27, 2/27, 1/54, and 1/216 for the rest, the six Cartesian, the twelve cubic edge-diagonal, and the eight cubic space-diagonal directions, respectively. The porosity ϕ, i.e., the fraction of void volume over total volume, is included to consider the presence of a porous medium and is derived from volume-averaging the LB equation [16]. A suitable form of the forcing term F_j is given by

$$F_j = \left(1 - \frac{\omega}{2}\right) w_j \rho \left(\frac{\underline{c}_j \cdot \underline{F}}{c_s^2} + \frac{\underline{u}\,\underline{F} : (\underline{c}_j\,\underline{c}_j - c_s^2 \underline{\underline{I}})}{c_s^4 \phi} \right) .$$

The cumulant collision operator is a multiple relaxation time operator, which relaxes cumulants with individual rates towards their equilibrium [14]. Cumulants are quantities of the Laplace-transformed discrete PPDF from time-velocity space $\underline{\xi}$ into the frequency-velocity space $\underline{\Xi} = \{\Xi, \Upsilon, Z\}$

$$C_{\alpha\beta\gamma} = c^{-\alpha-\beta-\gamma} \frac{\partial^\alpha \partial^\beta \partial^\gamma}{\partial \Xi^\alpha \partial \Upsilon^\beta \partial Z^\gamma} \ln(F(\underline{\Xi})) \bigg|_{\underline{\Xi}=\underline{0}} , \text{with} \quad F(\underline{\Xi}) = \mathcal{L}\{f(\underline{\xi})\} = \int_{-\infty}^{\infty} f(\underline{\xi}) e^{-\underline{\Xi} \cdot \underline{\xi}} d\underline{\xi} \,.$$

The collision in cumulant space reads

$$C^*_{\alpha\beta\gamma} = C_{\alpha\beta\gamma} - \omega_{\alpha\beta\gamma}(C_{\alpha\beta\gamma} - C^{eq}_{\alpha\beta\gamma}),$$

where $C^{eq}_{\alpha\beta\gamma}$ is the Maxwellian equilibrium in cumulant space and $\omega_{\alpha\beta\gamma}$ is the corresponding relaxation frequency. Following the nomenclature of [14], all relaxation rates but ω_1 are set to unity. The propagation step as well as boundary conditions are performed after transforming the post-collision cumulants back into momentum space. Local grid refinement techniques are employed to reduce the number of grid points and thus the computational effort. Here, the method of Dupuis and Chopard [17] is applied, in which different relaxation frequencies are used for different levels of refinement. To account for compressibility effects an acoustic scaling is applied such that the computational time step scales with the grid spacing $\Delta t \sim \Delta x$. From eq. (2) follows, that

$$\nu_{eff} = \Delta t c_s^2 \left(\frac{1}{\omega_{BGK}} - \frac{1}{2} \right) .$$

To keep the viscosity constant across the grid refinement interface, the relaxation frequency is scaled correspondingly to Δt. The no-slip boundary condition is implemented through an interpolated bounce-back scheme [18] allowing for a second order accurate representation of arbitrary shaped geometries.

Simultaneously resolving the scales of a turbulent flow around a realistic landing gear setup and those in the porous micro-structure is computational very expensive. Therefore, the volume averaging as shown in eq. (3) is introduced and the forcing term $\underline{F}$ describes a drag force acting on the flow through a porous material. It is modeled by a Forchheimer-extended Darcy equation

$$\underline{F} = \mathrm{C}_1 \underline{u} + \mathrm{C}_2 |\underline{u}| \underline{u}, \tag{4}$$

where C_1 and C_2 are unknown parameters of the model, which are characteristic properties of a specific porous material for a certain range of operation points, i.e., bulk velocity. These are obtained from calibration using reference data from experimental measurements or micro-structure resolving simulations.

B. Ffowcs Williams and Hawkings method

The Ffowcs Williams and Hawkings (FWH) equation [19] is an exact rearrangement of the Navier-Stokes equations, i.e., the conservation of mass, momentum, and energy

$$\begin{aligned} \left(\frac{\partial^2}{\partial t^2} - c_s^2 \frac{\partial^2}{\partial x_i^2} \right) (H(s)\rho') = \frac{\partial^2}{\partial x_i x_j} (T_{ij} H(s)) - \frac{\partial}{\partial x_i} (F_i \delta(s)) + \frac{\partial}{\partial t} (Q \delta(s)) \\ T_{ij} &= \rho u_i u_j + P_{ij} - c_s^2 \rho' \delta_{ij} && \text{(Quadrupole term)} \\ F_i &= (P_{ij} + \rho u_i (u_j - v_j)) \frac{\partial s}{\partial x_j} && \text{(Dipole term)} \\ Q &= (\rho_\infty v_i + \rho (u_i - v_i)) \frac{\partial s}{\partial x_i} && \text{(Monopole term)}, \end{aligned} \tag{5}$$

where δ_{ij} is the Kronecker delta, $\underline{\underline{P}} = p\delta_{ij}$ is the compressive stress tensor, ρ' is the perturbed density, and $H(\cdot)$ is the Heaviside step function. The support function $s = 0$ defines the FWH permeable surface. It takes positive values only outside of the volume enclosed by this surface, where the solution of the acoustic field is desired. The FWH surface is moving with the velocity $\underline{v}$.

Following Lockard [20], the FWH equation is transformed into frequency domain yielding a simpler formulation that can be solved more efficiently than in time domain. Therefore, a uniform rectilinear motion of the surface s is assumed before applying a Galilean transformation and a Fourier transformation. The final governing equations consist of two surface integrals and one volume integral and reads

$$\begin{aligned} H(s) c_s^2 \rho'(\underline{y_o}, \omega) = &- \oint_{s=0} i\omega Q(\underline{y_s}, \omega) G(\underline{y_o}; \underline{y_s}) dA - \oint_{s=0} F_i(\underline{y_s}, \omega) \frac{\partial G(\underline{y_o}; \underline{y_s})}{\partial y_{s,i}} dA \\ &- \int_{s>0} T_{ij}(\underline{y_s}, \omega) H(s) \frac{\partial^2 G(\underline{y_o}; \underline{y_s})}{\partial y_{s,i} \partial y_{s,j}} \underline{dy_s} , \end{aligned} \tag{6}$$

with the angular frequency ω and the Green's function $G(\cdot;\cdot)$. The source and observer coordinates are given by$\underline{y_s}$ and $\underline{y_o}$. If the volume enclosed by the FWH surface contains all significant acoustic quadrupole sources represented by the Lighthill stress tensor T_{ij}, a good approximation is to neglect the calculation of the volume integral as it is also done in the present study. Input data provided in the time domain is transformed into frequency space by using a Fast Fourier Transformation (FFT). To avoid spectral leakage, a modified Hanning window function [20] is applied. By performing an inverse FFT on the predicted sound pressure values, pressure signals in time can be obtained at any observer coordinates.

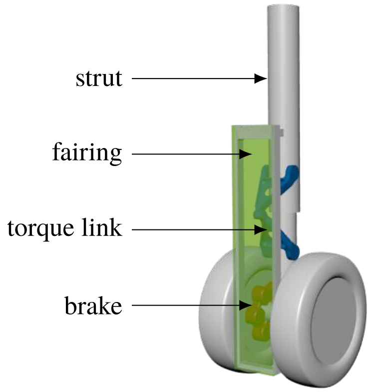

Fig. 1 Landing gear featuring brakes (red), torque link (blue), and fairing (green). The fairing is replaced by different kind of materials. Each feature including the fairings' holder is removable.

Table 1 LG geometry and flow parameters.

Wheel diameter D	150 mm
Upper strut diameter	0.24 D
Distance axle-wall	2.33 D
Outer wheel base	0.95 D
Fairing to strut distance	0.37 D
Fairing height	1.8 D
Fairing width	0.36 D
Mach number M_∞	0.10198
Wheel Reynolds number Re_D	346,306
Upper strut Reynolds number Re_S	83,113

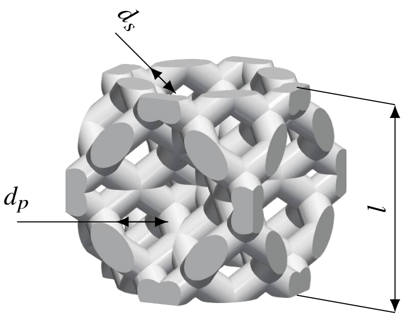

Fig. 2 Unit cell of the diamond lattice structure.

Table 2 Geometry of the diamond lattice structure and modeling parameters for the two porous fairings.

Abbreviation	*DL2.5*	*DL6.4*
Size of unit cell l	2.5 mm	6.4 mm
Fairing thickness L_f	2 l	1 l
Porosity ϕ	61.7 %	
Pore diameter d_p	0.1888 l	
Strut diameter d_s	0.1648 l	
C_1 [1/s]	-4,431	-833
C_2 [1/m]	-15,320	-4,060

IV. Geometry and computational setup

A two-wheel nose landing gear with a wheel diameter of $D = 150$ mm approximately corresponding to a 1:7 scale real nose LG is subject of the present study. It has a simplified geometry featuring brakes, a torque link, and a detachable fairing, as shown in fig. 1. The fairing is placed $0.37D$ in front of the strut having a height of $1.8D$ and a width of $0.36D$ covering the torque link, parts of the brakes, and the lower strut. The LG mounted on a flat plate is investigated at a wheel based Reynolds number of $Re_D \approx 346,000$ and a freestream Mach number of $M_\infty \approx 0.1$. The geometric parameters as well as the flow conditions are summarized in table 1.

Three different kinds of fairings are investigated, i.e., a solid and two porous fairings. The porous material is constructed by clustering multiple units of the diamond lattice structure shown in fig. 2. Each of these cells fits in a cubic box with an edge length of l. It consists of struts with a diameter of $d_s \approx 0.18l$ that are oriented with an angle of 60° in space to each other, resulting in a pore diameter of $d_p \approx 0.16l$ and a porosity of $\phi = 61.7\%$. Two fairings with different cell sizes and fairing thickness are investigated. Due to the large discrepancy of length scale between flow structures inside of the porous material and around the landing gear the material is modeled by volume-averaging as described in section III.A. The model parameters are obtained through calibration against pressure drop results from numerical simulations as well as from experimental data of Delft University of Technology and given in table 2.

The computational domain has a total extent of $130D \times 65D \times 32.5D$. The physical relevant part of the domain excluding a sponge area, where artificial viscosity is introduced to damp waves reflected back into the domain, is $80D \times 40D \times 20D$. The domain is discretized with a Cartesian grid, where the grid spacing on a refinement level r is given by $\Delta x_r = L/2^r$. Here, Δx_0 represents the length of a cubic bounding box of the computational domain with a length of $L = 130D$. The grid is refined at refinement patches as shown in fig. 3 starting from a refinement level of $r_{min} = 9$. At the LG's surface a boundary refinement within a thickness of $0.02D$ on the maximum refinement level

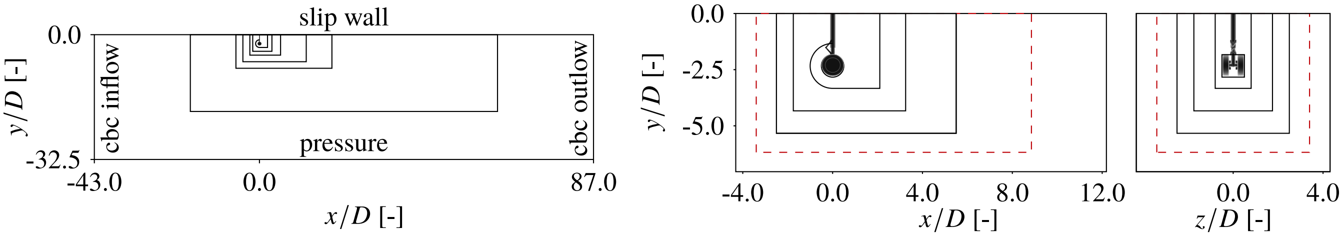

Fig. 3 Numerical setup of the CFD/CAA flow simulation. 2D slices showing the dimension of the refinement patches in black lines (–). On the left, a slice of the complete domain starting with a refinement level of 9 is shown. The two figures on the right show details starting with a refinement level of 12. In addition, the location of the FWH permeable surface is represented by a dashed red line (- ·),

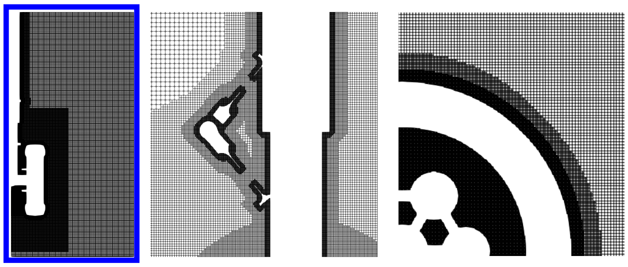

Fig. 4 Details of the grid refinement around the wheel, torque link, and brakes for the grid. Only every second grid point is shown.

Table 3 Properties of the surface grid and the temporal sampling of the FWH method's input data.

Δx_{fwh}	0.03 D
noElements	1,389,606
$\Delta t_{sampling}$	1 / 124kHz
$T_{sampling}$	27 / 0.2kHz
noSampling	16,384

corresponding to a grid resolution of $\Delta x_{max} = 1/1008D$ is applied. The transition to the next patch refinement level is created with at least 10 layers of cells, see fig. 4. This yield a total number of 705-850 million grid points and a computational time step of $\Delta t = 2.5 \cdot 10^{-7} s$. The LG surface is represented by a no-slip interpolated bounce-back boundary condition, whereas the mounting plate is considered simplified as a slip wall such that the boundary layer on the mounting plate is not resolved. The in- and outflow are described by non-reflecting characteristic boundary conditions extending the work of Izquierdeo and Fueyo [21] into three space dimensions. By solving the local one-dimensional inviscid (LODI) equations, which resemble the Euler equations without transverse derivative terms, waves being reflected back into the domain are mitigated. The determined macroscopic state is set through the corresponding equilibrium state. The remaining boundaries are defined by pressure equilibrium boundary conditions, i.e., the velocity is extrapolated from the interior domain, while the pressure/density is prescribed to be at ambient conditions. The presented setup is validated in [10] against experimental measurements provided by Delft University of Technology.

To predict the acoustic far field by the FWH method, time resolved flow field data is sampled during the LB solver run on a FWH surface. The surface position is depicted in fig. 3. It is discretized using a uniform right-angled trianglular grid with a maximum edge length of the underlying CFD grid of $\Delta x_{fwh} = 0.03D$. Thus, an acoustic wave with a frequency in the experiment of $9kHz$ is resolved with more than 8 grid points. The data is sampled with a frequency of $124kHz$ over a period of $T_{sampling} = 27/(0.2kHz)$. Table 3 summarizes the sampling settings and the details of the FWH surface grid.

V. Turbulent flow field around the landing gear

In this section, the influence of the different fairings on the turbulent flow field is discussed and the numerical approach of the treatment of the porous fairings as described in section III.A is verified. Therefore, comparisons with experimental data of *Delft University of Technology* (TUD) are provided. The corresponding experimental setup is explained in our previous study [10].

The instantaneous velocity field computed for the two reference configurations, i.e., the baseline LG and the baseline LG with a solid fairing, is visualized on isovolumes of the Q-criterion [22] in fig. 5. Both velocity fields are characterized by detached flows resulting in a turbulent wake. Due to the shielding properties of the solid fairing, vortical structures

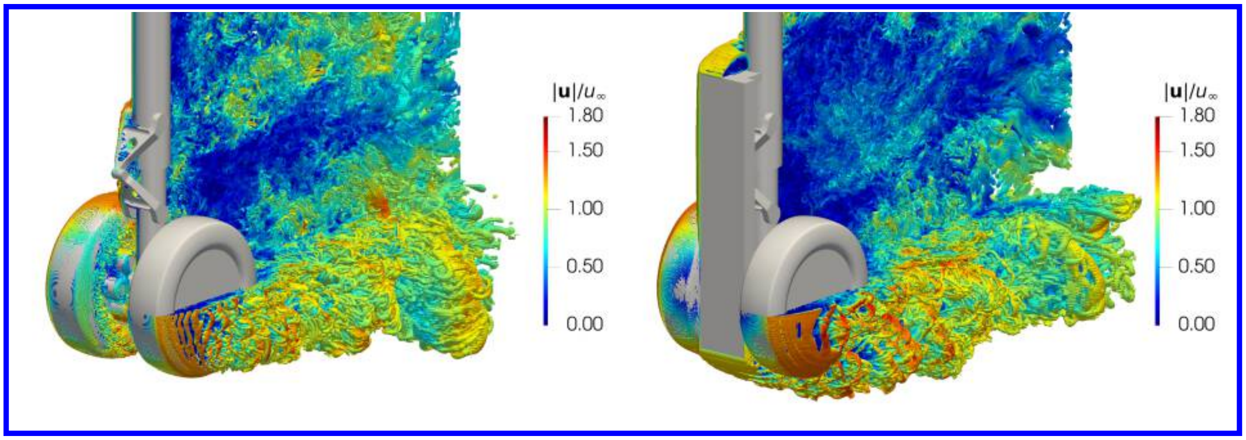

Fig. 5 Instantaneous velocity magnitude field on isovolumes of Q-criterion for the baseline (left) and baseline with solid fairing (right) configurations.

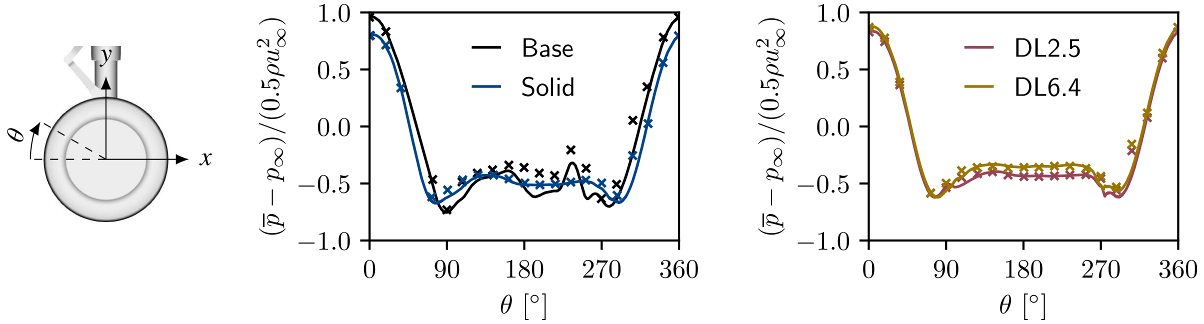

Fig. 6 Mean pressure circumferential distribution over the left LG wheel for the four configurations. The corresponding experimental results are given by crosses of the same color. The coordinate system is sketched on the left.

forming at the torque link interacting downstream with the strut as well as the highly turbulent flow in the region of the brakes are mitigated. Therefore, at the top of the fairing and in front of the strut an additional vortex forms. Also, the flow around the wheel is influenced by the lateral flow acceleration such that the separations at the outside of the wheels are amplified. In fig. 6, the pressure distribution over the left wheel for the four configuration is plotted. It fairly reproduces experimental measurements. Deviation from the experiment are observable for the baseline configuration. At this point it must be noted that in the experiment a zig-zag transition strips are added on the wheel at an angle of $\theta = \pm 60^\circ$, but left unconsidered in the numerical simulations. The pressure loss at the rear of the wheel is slightly lowered for the porous fairings compared to the solid one, whereas the points of lowest pressure move forward for all fairing configurations compared to the non-fairing baseline. The mean field of the streamwise velocity component $\overline{u}$ is extracted on a xz-slice through the LG axle and shown in fig. 7 for the four configurations. Considering the length and width of wake sections shown, the configurations agree very well with the experimental results. With increasing porosity of the fairing the separation on the wheel becomes larger and the LG's wake becomes wider. On the same slice the root mean square (RMS) field of the fluctuating velocity component $\mathrm{RMS}(u')$ is given in fig. 8. Slight discrepancy is observed for the baseline configuration between the numerical and experimental results as the flow coming from the wheels is stronger fluctuating in the numerical simulation. The configurations with fairing match very well with the experimental measurements. With increasing porosity of the fairing applied, the $\mathrm{RMS}(u')$ value in this slice grows around the wheels as well as in the center of the wake. In fig. 9, a more quantitative comparison is given by plotting the mean and RMS values extracted on specific lines, namley, the x-axis and a line parallel to the z-axis located downstream at $x/D = 1.13$ reinforcing the previous observations.

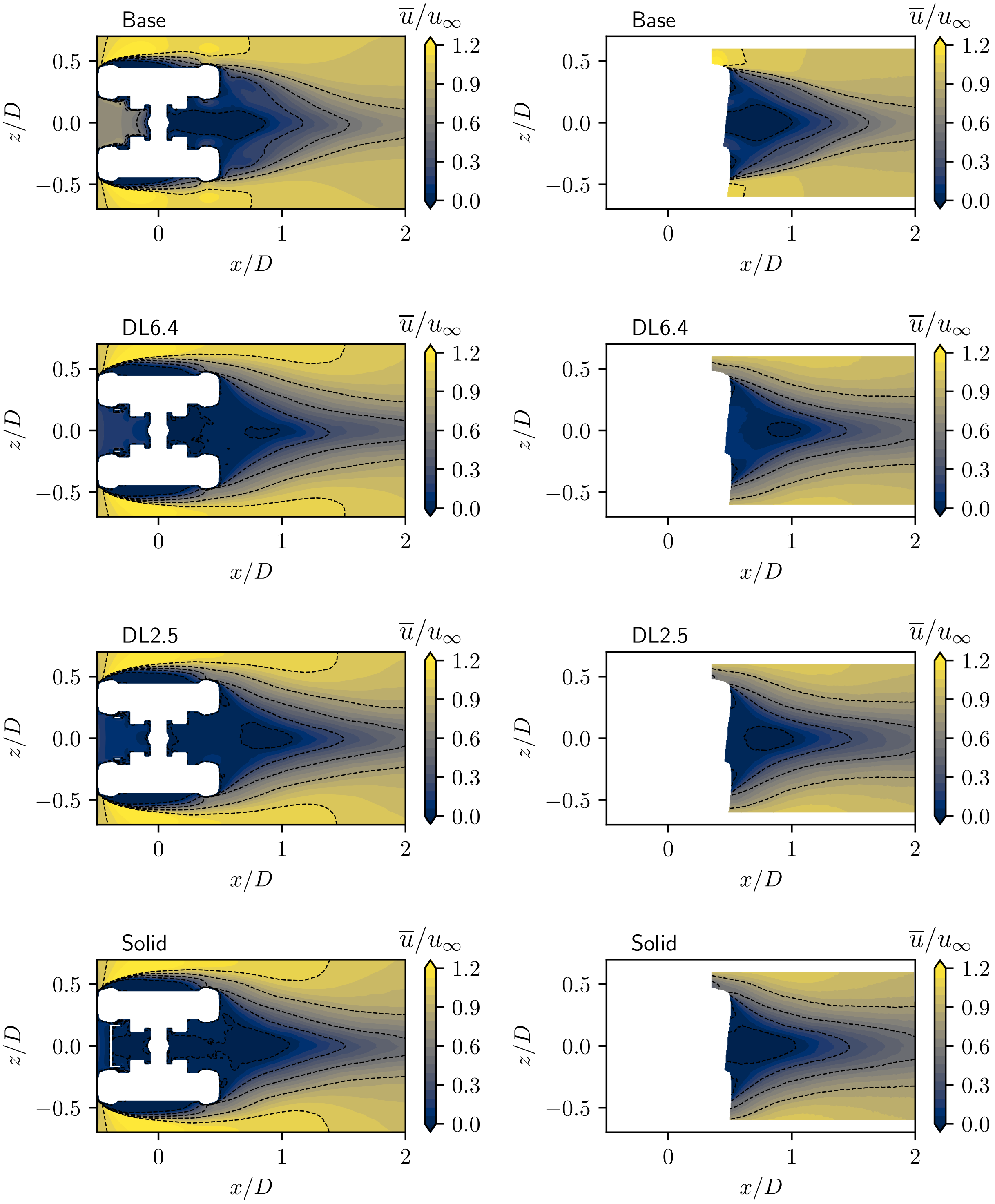

Fig. 7 **Mean field of the streamwise velocity on an xz-slice through the LG axle. The numerical results (left) and the experimental results of Delft University of Technology (right) are shown for the four configurations with decreasing fairing porosity from top to bottom row, i.e., Base, DL6.4, DL2.5, and Solid.**

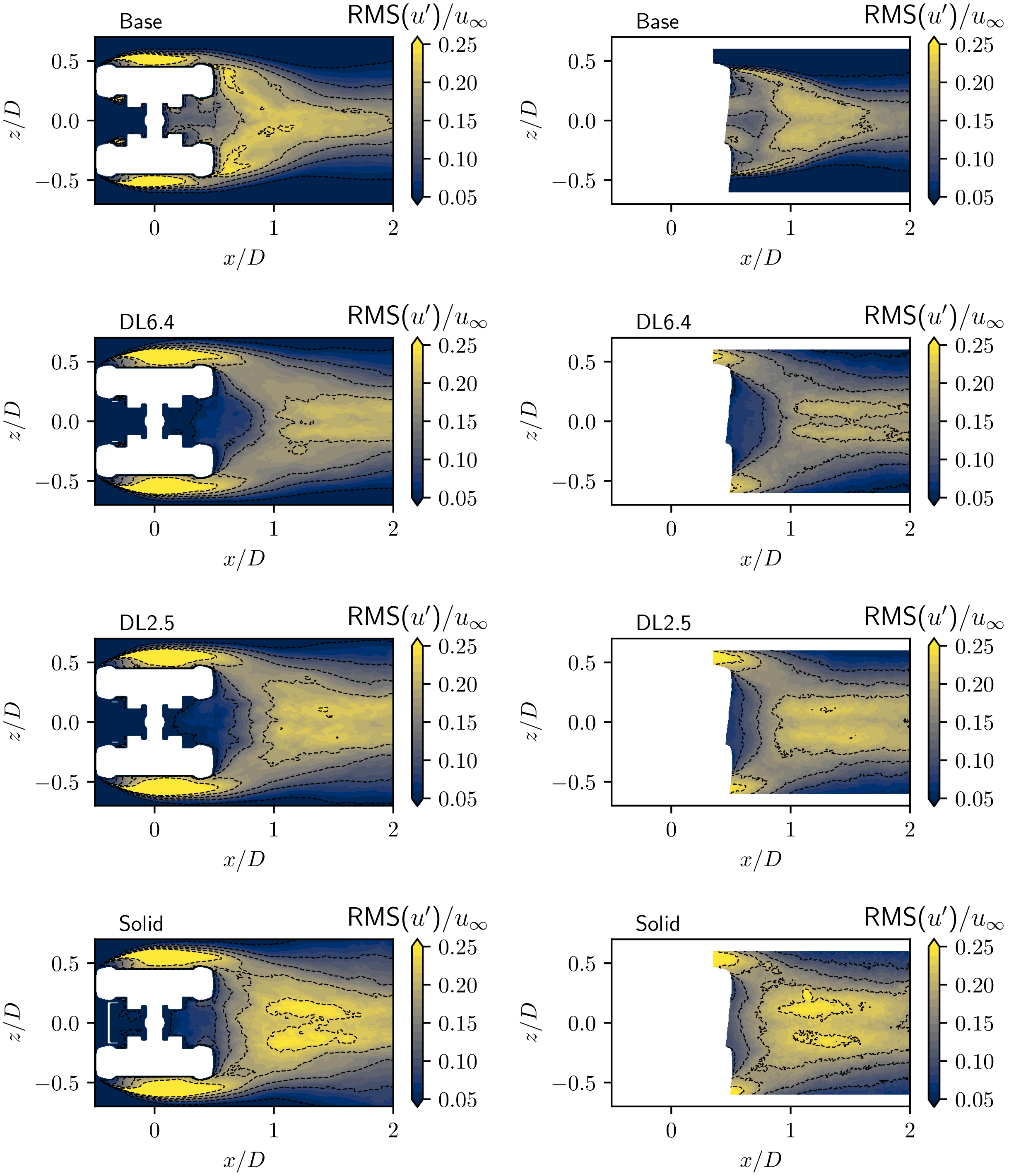

Fig. 8 Root mean square field of fluctuating streamwise velocity on an xz-slice through the LG axle. The numerical results (left) and the experimental results of Delft University of Technology (right) are shown for the four configurations with decreasing fairing porosity from top to bottom row, i.e., Base, DL6.4, DL2.5, and Solid.

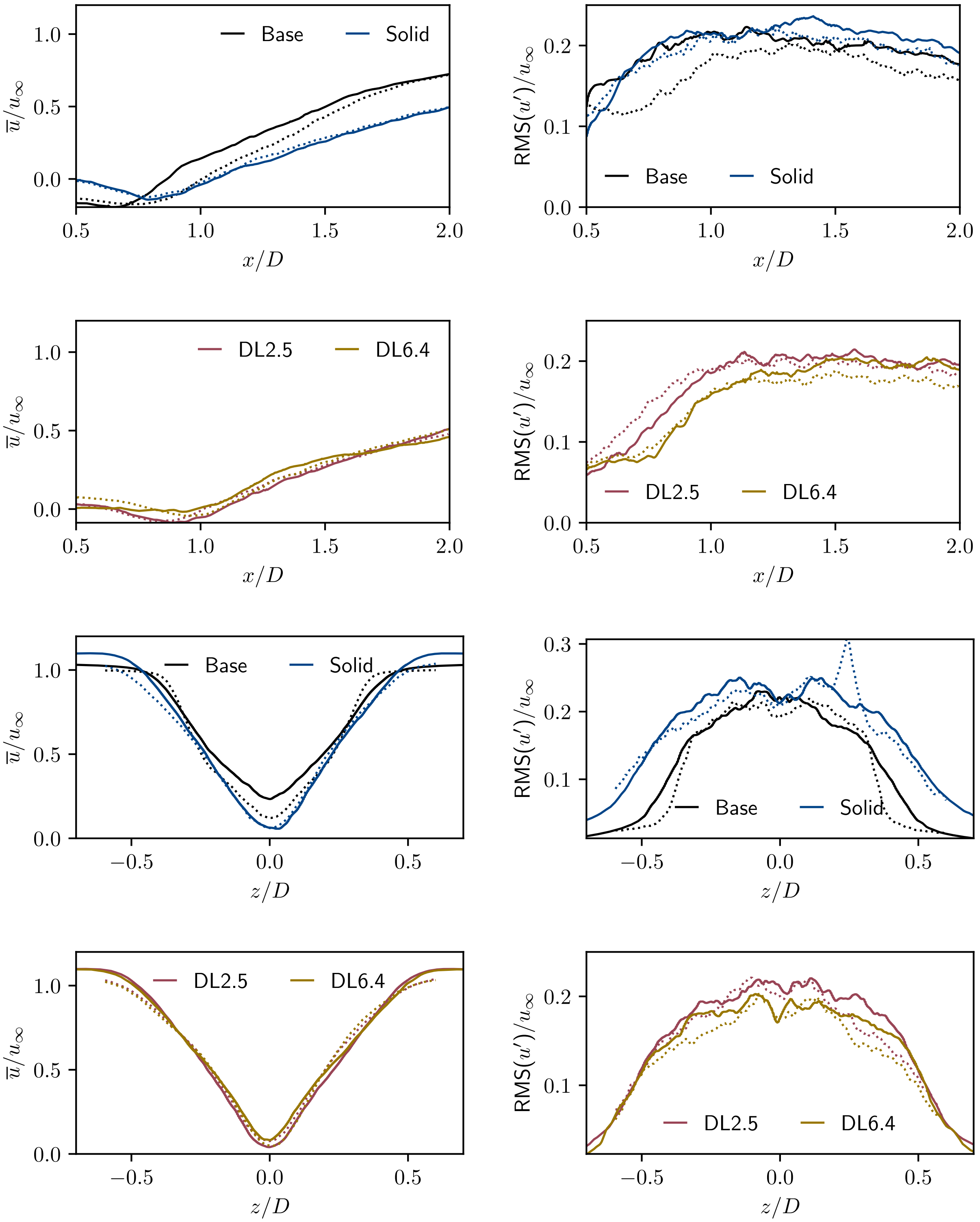

Fig. 9 Mean streamwise velocity (left) and root mean square of the fluctuating streamwise velocity (right) over two lines are shown for the four configurations. In the first two rows the x-axis and in the last two rows a line parallel to the z-axis located downstream at $x/D = 1.13$ are regarded. The corresponding experimental results are given by dotted lines of the same color.

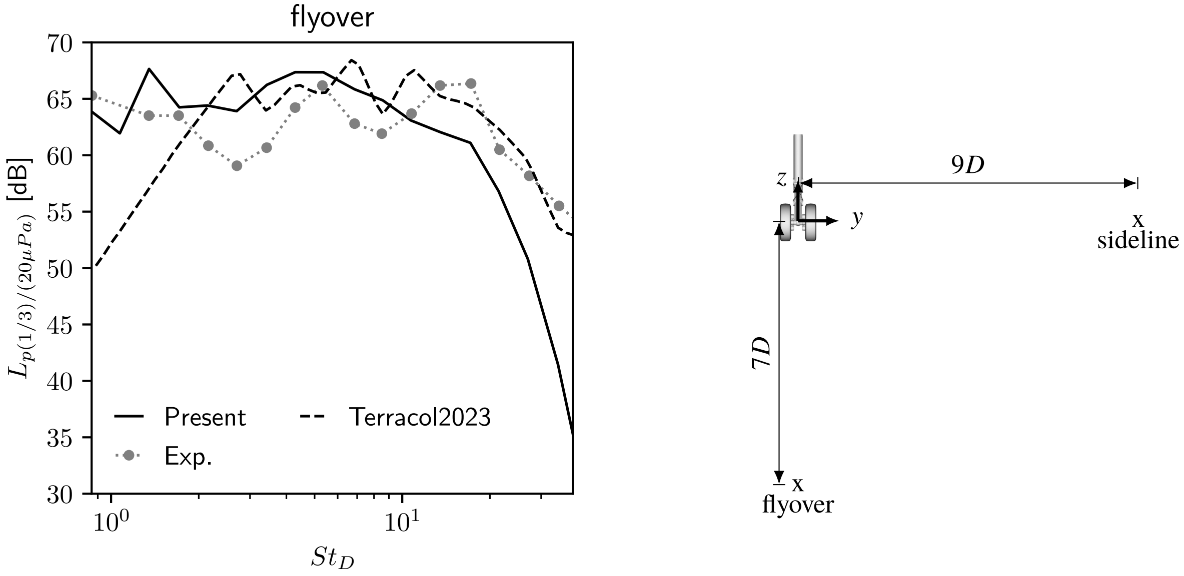

Fig. 10 Sound pressure level filtered in one-third octave bands at the sideline microphone position for the base line configuration showing results from the present study as well as from Terracol et al. [23] and the experiment. The location of the microphones used in this study are sketched on the right.

VI. Noise mitigation properties of the investigated fairings

As shown in the previous section the presented numerical approach including the modeling of the porous fairings is capable of reproducing the flow field statistics obtained from experimental PIV measurements. In this section the acoustic far field generated by the different configurations is presented and noise source are discussed.

Two microphones positioned in a distance of $7D$ fylover and $9D$ sideline as sketched in fig. 10 are considered in the following. First, the sound pressure levels predicted by the FWH calculation are compared to experimental results as well as to an existing numerical study of Terracol et al. [23] for the baseline configuration, see fig. 11. The numerical result differ from the experimental ones by approx. 5 dB with a comparable error as in the referred study showing a lower cut-off frequency. This strong discrepancy allows a comparison of the noise reduction capabilities of the applied fairings only on a qualitative point of view. However, in fig. 11 the predicted sound pressure levels of the different configuration are plotted for the two microphones. All fairings show a noise reduction of approx. 3 dB over a wide range of frequencies. At the sideline position the porous fairings perform similar as the solid version, while in the flyover location the *DL6.4* fairing show better mitigation in the mid frequency range.

The distribution of wall pressure fluctuations on the LG surface, see fig. 12, are a known indicator for noise sources. For the baseline configuration high fluctuations are present on the torque link and the strut, where the torque link's wake is impinging on, as well as on the inside of the wheels and brakes. Installing the solid fairing effectively reduces these kind of fluctuations. Therefore, additional noise sources are arising at the strut next to the fairing's junction. The two porous fairings show similar shielding properties. However, the fluctuations in the brake region are slightly lower as in the solid version. In the region behind of the fairing junction, the fluctuations are lower as the fairing porosity increases, which is in agreement with the sound pressure levels.

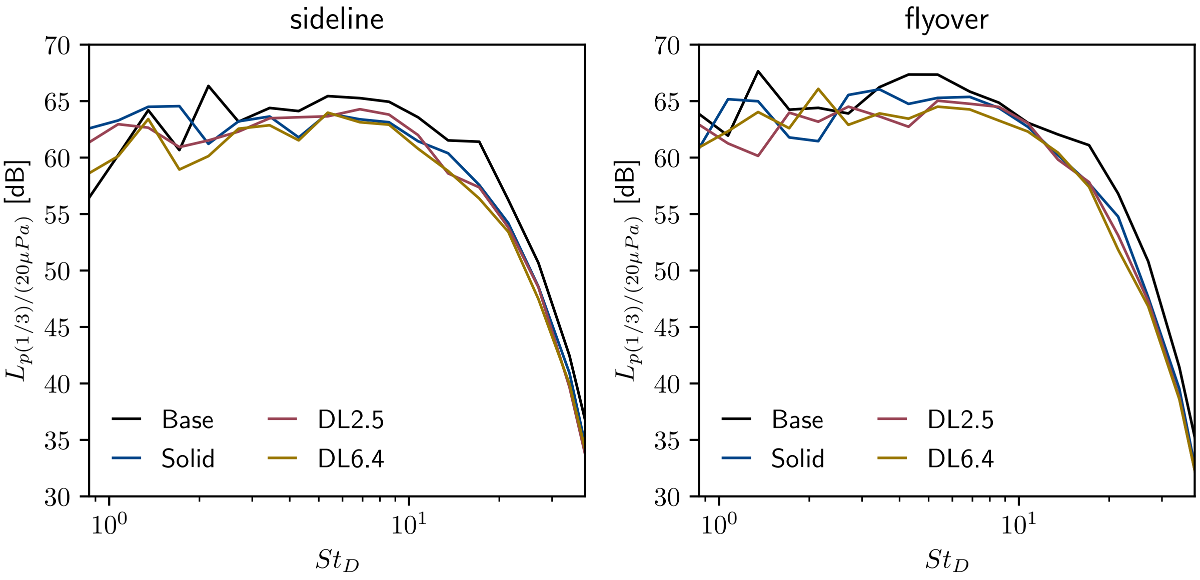

Fig. 11 Sound pressure level filtered in one-third octave bands at the two microphone positions for the different landing gear configuration.

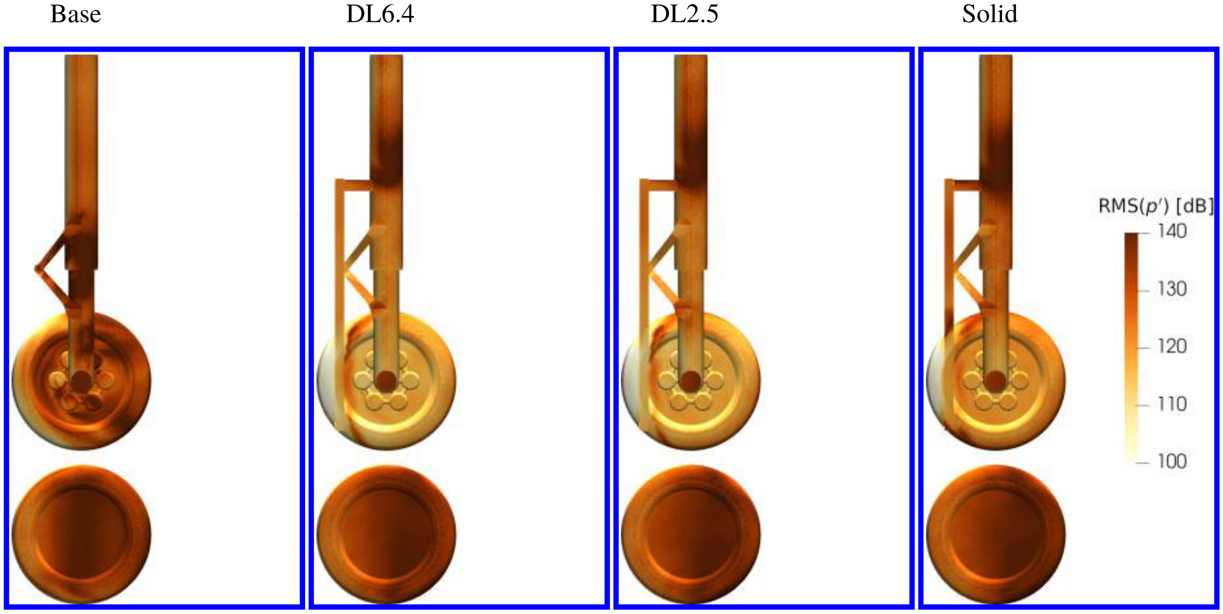

Fig. 12 Root mean square of the fluctuating wall pressure in dB (p_{ref} = 20 μPa). For a better visualization the left wheel is shifted downwards.

VII. Conclusion and outlook

The present work continued the study of a simplified landing gear with an upstream installed solid fairing [10]. Two porous fairings consisting of the diamond-lattice structure are considered to be investigated regarding their noise mitigation properties compared to the equivalent solid fairing. The flow and acoustic near field is computed by a cumulant based lattice Boltzmann method. Here, the effect of the porous materials on the flow field is modeled by a Forchheimer-extended Darcy model calibrated through numerical and experimental pressure drop results to circumvent resolving the flow in the porous micro-structures.

Flow field statistics obtained from the simulations show a very well agreement with the experimental PIV data demonstrating the capability of the numerical approach chosen. However, comparing the predicted far field sound pressure levels against experimental reference shows a discrepancy of up to 5 dB. The applied porous fairings show slightly improved noise mitigation properties compared to its solid equivalent.

Better acoustic results are expected to be obtained with an optimized positioning of the FWH permeable grid points, i.e., sampling in a region of higher frequency resolution. Considering an improved FWH formulation with the usage of quadrupole correction terms in the frequency domain could not be achieved for the recent conference but will be done in future work.

Acknowledgments

The project received funding from the European Union’s Horizon 2020 research and innovation programme within the project INVENTOR (*innovative design of installed airframe components for aircraft noise reduction*) listed under the grant agreement ID: 860538.

The authors address special thanks to the other teams of the INVENTOR consortium contributing definitions of the landing gear geometries, i.e., German Aerospace Center (DLR) and Dassault Aviation.

The authors gratefully acknowledge the Gauss Centre for Supercomputing e.V. (www.gauss-centre.eu) for funding this project by providing computing time on the GCS Supercomputer HAWK at Höchstleistungsrechenzentrum Stuttgart (www.hlrs.de).

References

[1] Dobrzynski, W., “Almost 40 Years of Airframe Noise Research: What Did We Achieve?” *J. Aircraft*, Vol. 47, No. 2, 2010, pp. 353–367. https://doi.org/10.2514/1.44457.

[2] Manoha, E., Bulté, J., and Caruelle, B., *Lagoon : An Experimental Database for the Validation of CFD/CAA Methods for Landing Gear Noise Prediction*, 2008. https://doi.org/10.2514/6.2008-2816.

[3] Sanders, L., Manoha, E., Khelil, S., and Francois, C., *LAGOON: New Mach Landing Gear Noise Computation and further analysis of the CAA process*, 2012. https://doi.org/10.2514/6.2012-2281.

[4] Casalino, D., Ribeiro, A., Fares, E., and Nölting, S., “Lattice–Boltzmann aeroacoustic analysis of the LAGOON landing-gear configuration,” *AIAA J.*, Vol. 52, No. 6, 2014, pp. 1232–1248. https://doi.org/10.2514/1.J052365.

[5] Ricciardi, T. R., Wolf, W. R., and Speth, R., “Acoustic Prediction of LAGOON Landing Gear: Cavity Noise and Coherent Structures,” *AIAA J.*, Vol. 56, No. 11, 2018, pp. 4379–4399. https://doi.org/10.2514/1.J056957.

[6] Coskun, O., McCarthy, P., and Ekmekci, A., *An Aeroacoustic Study of the Nose Landing Gear with Emphasis on Steering Actuators, Torque Link and Tow Hook*, 2020. https://doi.org/10.2514/6.2020-1726.

[7] Terracol, M., and Manoha, E., “Numerical Wire Mesh Model for the Simulation of Noise-Reduction Devices,” *AIAA J.*, Vol. 59, No. 3, 2021, pp. 987–1007. https://doi.org/10.2514/1.J059548.

[8] Murayama, M., Yokokawa, Y., Yamamoto, K., and Hirai, T., “Computational study of low-noise fairings around tire-axle region of a two-wheel main landing gear,” *Comput. Fluids*, Vol. 85, 2013, pp. 114–124. https://doi.org/https://doi.org/10.1016/j.compfluid.2012.11.001, international Workshop on Future of CFD and Aerospace Sciences.

[9] Merino-Martínez, R., Kennedy, J., and Bennett, G. J., “Experimental study of realistic low–noise technologies applied to a full–scale nose landing gear,” *Aerosp. Sci. Techn.*, Vol. 113, 2021, p. 106705. https://doi.org/https://doi.org/10.1016/j.ast.2021.106705.

[10] Gondrum, M., Niemöller, A., Meinke, M., Schröder, W., Carpio, A., Ragni, D., and Avallone, F., "Landing Gear Noise Mitigation by an upstream installed Fairing," *28th AIAA/CEAS Aeroacoustics Conference*, American Institute of Aeronautics and Astronautics, 2022. https://doi.org/10.2514/6.2022-2847.

[11] Enskog, D., "Kinetische Theorie der Vorgänge in mässig verdünnten Gasen." Ph.D. thesis, 1917.

[12] Guo, Z., Zheng, C., and Shi, B., "Discrete lattice effects on the forcing term in the lattice Boltzmann method," *Phys. Rev. E*, Vol. 65, 2002, p. 046308. https://doi.org/10.1103/PhysRevE.65.046308, URL https://link.aps.org/doi/10.1103/PhysRevE.65.046308.

[13] Bhatnagar, P. L., Gross, E. P., and Krook, M., "A Model for Collision Processes in Gases. I. Small Amplitude Processes in Charged and Neutral One-Component Systems," *Phys. Rev.*, Vol. 94, 1954, pp. 511–525. https://doi.org/10.1103/PhysRev.94.511.

[14] Geier, M., Schönherr, M., Pasquali, A., and Krafczyk, M., "The cumulant lattice Boltzmann equation in three dimensions: Theory and validation," *Comp. Math. Applics*, Vol. 70, No. 4, 2015, pp. 507–547. https://doi.org/10.1016/j.camwa.2015.05.001.

[15] Hou, S., Sterling, J., Chen, S., and Doolen, G., "A Lattice Boltzmann Subgrid Model for High Reynolds Number Flows," *Fields Inst. Commun.*, Vol. 6, 1996, pp. 151–166.

[16] Guo, Z., and Zhao, T. S., "Lattice Boltzmann model for incompressible flows through porous media," *Phys. Rev. E*, Vol. 66, 2002, p. 036304. https://doi.org/10.1103/PhysRevE.66.036304.

[17] A., D., and Chopard, B., "Theory and applications of an alternative lattice Boltzmann grid refinement algorithm," *Phys. Rev. E*, Vol. 67, 2003, p. 066707. https://doi.org/10.1103/PhysRevE.67.066707.

[18] Bouzidi, M., Firdaouss, M., and Lallemand, P., "Momentum transfer of a Boltzmann-lattice fluid with boundaries," *Phys. Fluids*, Vol. 13, No. 11, 2001, pp. 3452–3459. https://doi.org/10.1063/1.1399290.

[19] Williams, J. E. F., and Hawkings, D. L., "Sound generation by turbulence and surfaces in arbitrary motion," *Phil. Trans. R. Soc. London A*, 1969, pp. 321–342.

[20] Lockard, D., "An efficient, two-dimensional implementation of the Ffowcs Williams and Hawkings equation," *J. Sound Vibr.*, Vol. 229, No. 4, 2000, pp. 897–911. https://doi.org/10.1006/jsvi.1999.2522.

[21] Izquierdo, S., and Fueyo, N., "Characteristic nonreflecting boundary conditions for open boundaries in lattice Boltzmann methods," *Phys. Rev. E*, Vol. 78, 2008, p. 046707. https://doi.org/10.1103/PhysRevE.78.046707.

[22] Hunt, J., Wray, A., and Moin, P., "Eddies, streams, and convergence zones in turbulent flows," *Studying turbulence using numerical simulation databases, 2. Proceedings of the 1988 summer program*, 1988, pp. 193–208.

[23] Terracol, M., Manoha, E., Manueco, L., Avallone, F., Ragni, D., and Carpio, A., *Numerical Simulations of a Landing Gear with Flow Through Fairings for Noise Mitigation*, American Institute of Aeronautics and Astronautics, 2023. https://doi.org/10.2514/6.2023-4173.